Shear-induced migration and axial development of particles in channel flows of non-Brownian suspensions

Ahmadreza Rashedi[1,2] | Mohammad Sarabian[1] | Mohammadhossein Firouznia[1] |
Dallas Roberts[1] | Guillaume Ovarlez[2] | Sarah Hormozi[1,3]

[1]Department of Mechanical Engineering, Ohio University, Athens, Ohio

[2]University of Bordeaux, CNRS, Solvay, LOF, UMR 5258, Pessac, France

[3]Robert Frederick Smith School of Chemical and Biomolecular Engineering, Cornell University, Ithaca, New York

Correspondence
Sarah Hormozi, Robert Frederick Smith School of Chemical and Biomolecular Engineering, Cornell University, Ithaca, NY 14853.
Email: hormozi@cornell.edu

Abstract

We present an experimental study on the shear-induced migration and axial development of particles in the channel flows of non-Brownian suspensions. The suspending fluid is Newtonian. We investigate fracturing flows with a Hele-Shaw type scaling through building a unique channel setup and an advanced optical system. The local particle concentration profiles are measured via the refractive-index matching technique for a wide range of bulk volume fraction, that is, $0.1 \leq \bar{\phi}_b \leq 0.5$. Simultaneously, the particle image velocimetry is performed to determine the velocity profile of the particle phase. We compare our experimental results with the available two-phase continuum frameworks and show discrepancies and similarities in the fully developed and axial development of the solid volume fraction profiles. We discuss directions in which the continuum frameworks require improvements.

KEYWORDS

fracturing flows, non-Brownian suspensions, shear-induced migration

1 | INTRODUCTION

Slurries are suspensions of particles in a viscous liquid. They are found in natural settings, such as landslides, mudslides, and submarine avalanches, and industrial settings, such as in petroleum industries and tailings from mining operations. In all of these examples, the dispersion of solids affect the rheology and consequently, the flow dynamics. The objective of this study is to provide experimental data on the shear-induced solid inhomogeneities in flow scenarios with the Hele-Shaw and thin-film type scalings. Notably, our focus is on the fracturing flows of non-Brownian suspensions of Newtonian fluids, for which thermal fluctuations are negligible.

The US is the largest producer of natural gas and oil. Around 50% of the oil and natural gas production in the United States is the outcome of hydraulic fracturing.[1,2] Improving fracturing techniques to enhance oil and gas production is therefore of considerable industrial and economic interest. In hydraulic fracturing, a suspension consisting of sand particles (proppant) and a viscous liquid is engineered.[3] Sometimes fractures are created in the reservoir via an explosion.[4] Then,

the fractures are kept open by pumping the suspension with a high pressure all the way from the well to the fracture. The flow in the well is usually turbulent, and it becomes laminar as it divides into many branches of fractures. The grains will support the fracture when the pumping is stopped.[3] This method increases the permeability of the oil reservoir and consequently, the hydrocarbon's production. It is essential to understand the physical mechanisms underlying the dispersion of solids in fracturing flows to design new fracturing techniques and modify pumping schedules to achieve the maximum efficiency of the reservoir.

One of the recent fracturing methods that results in infinite reservoir conductivity is called the channel fracturing technique (CFT).[3] The concept behind this technology is to substitute the uniformly distributed grains of proppant (i.e., porous media) in the fracture by discrete pillars/slugs of proppant. Therefore, in CFT, the reservoir fluids flow through open channels held by proppant pillars instead of porous media as in conventional fracturing methods. It is known that the effective permeability of an open channel is much higher than that of a porous medium.[3] Therefore, the proper design of this technique to

achieve the open channel configuration revolutionizes the fracturing industries. We have recently provided a mathematical framework to estimate the axial dispersion of solids in CFT.[5] We showed that, to the leading order, the axial dispersion of the particle phase depends on the transverse distribution of the particles across the fracture induced by the shear. The phenomenon is called shear-induced migration, with a rich history of research that is explained in several papers.[6,7] Nonetheless, we provide a brief review here.

In particulate flows, the particles' distribution can be attributed to the hydrodynamics and multibody interactions of the particles. In a nonhomogeneous shear flow of Newtonian suspensions, it is observed that particles migrate from the high shear rate region to the low shear rate region,[8,9] that is, shear-induced migration. For pressure driven flows, particle migration from walls (zones of high shear rate) toward the center (low shear rate regions) has been observed by many researchers using different experimental techniques, such as nuclear magnetic resonance imaging, Laser-Doppler Velocimetry (LDV), and refractive index (RI) matching. Studies extend to boundary driven flows. In summary, several experimental measurements have been carried out in different configurations, such as cylindrical Couette cells,[8-16] pipes,[17-20] channels,[21,22] and two parallel disks.[13,15,23] By and large, the results demonstrate the migration of particles from the regions of higher shear rate to the regions of low shear rate.

Several modeling and computational approaches have been taken to explain the shear-induced migration of particles. On the computational front, techniques such as Stokesian dynamics, force coupling method, and immersed boundary method are used to provide understanding of the particles' distribution and its connection with the hydrodynamics and multibody interactions. For more information about the details of these numerical approaches, the reader is referred to the following recent work.[10,24-27] On the modeling front, at least two approaches have been taken to explain the shear-induced migration. The approach of Acrivos et al.[8,9] is essentially phenomenological in adding a diffusive term to the right-hand side of the continuity equation for solid phase continuum. The physical origin of this term is stochastic, meaning that different initial configurations of particles will result in different evolutions. The diffusive fluxes are induced by collisions, gradients in the relative viscosity of the suspension with respect to the solid volume fraction and Brownian motion (negligible for the fracturing flows that we consider).

Another approach has effectively been made that diffusive fluxes arise naturally from gradients in the stresses associated with the particle phase, which enter the solid phase continuity equation directly by considering the particle drag closure. This is the approach underlying the suspension balance model (SBM) of Brady and coworkers.[28-30] There exists rheological laws, constants and multipliers in any proposed theoretical or computational framework that should be determined from experimental measurements.

Recent advancement of the experimental techniques allowed researchers to provide well-resolved data on the distribution of particles in different shearing flow scenarios.[10,16,20,31] Besides, new measurements of particle-phase stresses are provided to the community, for example, .[32-35] We refer the reader to the recent review by Guazzelli and Pouliquen.[6] Moreover, due to the improvement of computational methods,[24-26,36] interface-resolved simulations of solid particles in Newtonian fluids revealed details of the underlying physics in suspension flows. In summary, it has been shown that the recent computational and experimental data cannot fully be explained by the available model frameworks.[8,9,30] Our recent effort in understanding the fracturing flows[5] has led us to contribute to the field.[10,37-41] This paper aims to add to the existing literature by providing well-resolved experimental data on the shear-induced migration and axial development of particles in channel flows of non-Brownian suspensions. This study, along with other recent data in the field, may serve as a basis for improving and refining available model frameworks for non-Brownian suspensions.

The main, novel contributions of our study are as follows. First, we briefly explain fracturing flows of Newtonian suspensions (Section 2). We design and build a unique setup with an optical system to measure the velocity and solid volume fraction profiles in channel flows of non-Brownian suspensions (Section 3). Second, we provide systematic measurements of the shear-induced migration of particles and the axial development of the solid volume fraction in the channel setup for both dilute and dense suspension flows (Section 4). We summarize our results and discuss the difference between our data and the prediction of the available model frameworks (Section 5).

2 | CHANNEL FLOWS OF STOKESIAN SUSPENSIONS

The present work is mainly experimental. However, we use the SBM model framework with a significant simplification over a fully three-dimensional problem to build the experimental setup and design the experimental matrix. The purpose is to estimate Stokesian flows in long and thin fractures. Here, we briefly explain the SBM model framework for our channel setup and analyze one of the simplifications. As far as a detailed review of the SBM framework is concerned, we refer the reader to the recent literature.[5,6,10,20]

2.1 | Designing a channel for migration experiments

The objective is to build a channel that resembles a thin and long fracture in an oil reservoir (typically the length to the width ratio is beyond 1,000) and to tune the fracturing suspension properties and the flow for the two-phase continuum framework to be held. Therefore, we require enough particles across the gap. Several dimensionless numbers are taken into account for scaling purposes. We study Stokesian suspensions, and we conduct experiments with negligible inertial effects at flow and particle scales.

We denote the ratio between the particle diameter ($\hat{d}_p$) and the channel gap ($\hat{D}$) by δ_p, which is of the order of (10^{-2}) to make sure that there exist enough particles across the gap to consider the suspension as a continuum medium. Another geometrical dimensionless number

is $\delta_l = \hat{D}/\hat{L}$, which shows the ratio between the gap and the length of the channel ($\hat{L}$). We build a channel with, small δ_l to resemble a fracture, assuring the concentration of solid reaches a fully developed value. It is noteworthy to mention at least two time scales exist in this problem, that is, the advective time scale and the diffusion time scale. The former time scale is the ratio of the channel's length to the average velocity. The diffusion time scale gives an estimate of the particles' migration across the gap, which is of the order of the average shear rate times the square particle diameter. We can show that the ratio of the advective time scale to the diffusion time scale is δ_l/δ_p^2, and it is of the order of 1 in our channel, assuring the solid volume fraction achieves fully developed.

Finally, we choose δ_h (the ratio between the gap and the height of the channel $\hat{H}$) to be small enough. Therefore, in the channel's central region, the flow is 2D and it is not affected by the top and bottom wall boundaries. Table 1 presents the dimensions, the flow rate, and the dimensionless numbers of the channel setup. $\hat{U}_0$ is the mean velocity at the channel entrance. We follow the work of Miller and Morris[42] to simplify the SBM framework for our channel flows and use their results for the comparison. It is noteworthy to mention that solving the full 3D problem numerically is beyond this experimental work scope.

2.2 | SBM equations in a channel flow

Here, we study density-matched Stokesian suspensions. Therefore, we neglect inertial and gravity effects. Below, we briefly present the SBM approach explained in Reference 42 to derive the system of equations that needs to be solved for modeling channel flows of non-Brownian suspensions.

In the SBM,[30,43-45] the gradient of particle normal stress causes the diffusive flux of particles. The transport equation for the solid volume fraction ϕ is as follows.[42]

$$\frac{\partial \phi}{\partial t} + \nabla \cdot [\phi \mathbf{u}] = -\nabla \cdot \left[\frac{d_p^{\,2}}{18\eta_f} f(\phi) \nabla \cdot \Sigma^p \right] \tag{1}$$

where u is the suspension velocity, Σ^p is the particle stress tensor, η_f is the viscosity of the Newtonian fluid, and $f(\phi)$ is the hindrance function:

$$f(\phi) = (1-\phi)^{\alpha} \tag{2}$$

In order to compute the distribution of the solid volume fraction, Equation (1) is solved together with the mass and momentum equation for the suspension flow:

$$\nabla \cdot u = 0 \tag{3}$$

$$\nabla \cdot \Sigma = 0 \tag{4}$$

where $\Sigma = \Sigma^f + \Sigma^p$ is the suspension stress tensor. The particle phase stress Σ^p and the fluid phase stresses Σ^f are:

$$\Sigma^p = -\Sigma_N^p + 2\eta_f \eta_p E \tag{5}$$

$$\Sigma^f = -P_f I + 2\eta_f E \tag{6}$$

where P_f is the pressure of the fluid phase, I is the identity tensor, E is the strain rate tensor, and Σ_N^p is the particle phase normal stress tensor which is rewritten as:

$$\Sigma_N^p = \eta_f \eta_N |\dot{\gamma}| Q \tag{7}$$

$$Q = \begin{bmatrix} 1 & 0 & 0 \\ 0 & \lambda_2 & 0 \\ 0 & 0 & \lambda_3 \end{bmatrix} \tag{8}$$

where η_N is the relative normal viscosity of the suspension, and $\eta_s = \eta_p + 1$ is the relative shear viscosity of the suspension.

These equations have been solved by Miller and Morris[42] using the finite-volume method with the rheological model proposed by Morris and Boulay[42] as a closure. The rheological laws of Morris and Boulay[43] are:

$$\eta_N = K_n (\phi/\phi_m)^2 (1-\phi/\phi_m)^{-2} \tag{9}$$

$$\eta_s = \eta/\eta_f = 1 + 2.5\phi(1-\phi/\phi_m)^{-1} + K_s(\phi/\phi_m)^2(1-\phi/\phi_m)^{-2} \tag{10}$$

with $K_n = 0.75$, $K_s = 0.1$, $\alpha = 4$, $\lambda_2 = 0.8$, $\lambda_3 = 0.5$, and $\phi_m = 0.6$.
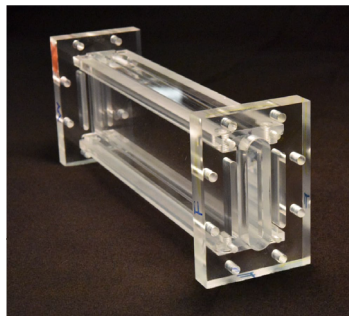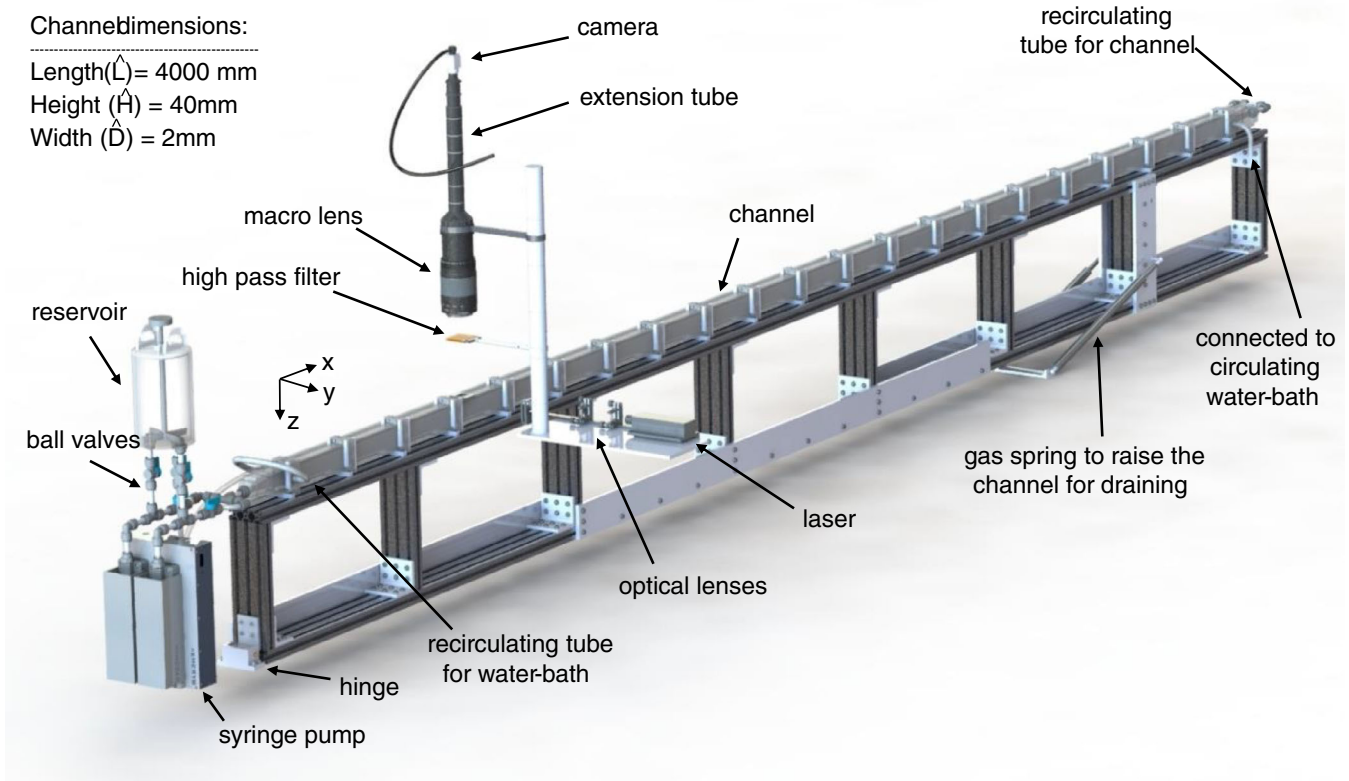
The results obtained for the steady-state solution by Miller and Morris[42] will be compared to our experimental results.

As discussed by Miller and Morris,[42] a simplified version of the transport equation can be solved provided the (a) flow throughout the conduit is steady (meaning that $\frac{\partial \phi}{\partial t} = 0$), and (b) flow can be considered as 2D (i.e., variations across z can be neglected). This is precisely achieved in our experiments thanks to the (a) suspension recirculation in the channel which allows reaching a steady state and (b) small width to height ratio of the channel. In these conditions, Equation (1) finally reduces to:

$$u_x \cdot \frac{\partial \phi}{\partial x} = -\frac{\partial}{\partial y} \left[\frac{d_p^{\,2}}{18\eta_f} f(\phi) \frac{\partial}{\partial y} \Sigma_{yy}^p \right] \tag{11}$$

We have solved numerically this equation together with the suspension momentum equation with the closures of Morris and Boulay[43] given above. We solve this nearly one-dimensional equation numerically. The equation is solved following Miller and Morris by computing progressively the velocity $U(y)$ when the solution marches through the channel. At each position y, $U(y)$ is computed from stress balance and from the current solution $\phi(y)$, while ensuring that the suspension flux remains constant. Note that the particle flux also remains constant. The steady-state volume fraction profiles and their axial development will be compared to the experimental results. Moreover, we also compare our experimental results with the fully 2D channel solution given by Miller and Morris.[42] It is noteworthy to mention that we compare the present work with the results of Miller

TABLE 1 Experimental parameters

$\hat{L}$ (mm)	$\hat{H}$ (mm)	$\hat{D}$ (mm)	$\hat{d}_p$ (mm)	$\hat{U}_0$ (mm/s)	$\hat{\eta}_0$ (Pa.s)
4,000	40	2	0.075–0.09	0.125	4.64
$\hat{\rho}_0$ (g/ml)	$\delta_l = \frac{\hat{D}}{\hat{L}}$	$\delta_h = \frac{\hat{D}}{\hat{H}}$	$\delta_p = \frac{\hat{d}_p}{\hat{D}}$	$Re = \frac{\hat{\rho}_f \hat{U}_0 \hat{D}}{\hat{\eta}_0}$	$Re_p = \frac{\hat{\rho}_f \hat{d}_p^2 \hat{\dot{\gamma}}}{\hat{\eta}_0}$
1.19	5×10^{-4}	0.05	~ 0.041	6.41×10^{-5}	1.09×10^{-7}

Channel dimensions:

Length ($\hat{L}$) = 4000 mm
Height ($\hat{H}$) = 40mm
Width ($\hat{D}$) = 2mm

camera

recirculating tube for channel

extension tube

macro lens

channel

high pass filter

reservoir

ball valves

connected to circulating water-bath

gas spring to raise the channel for draining

laser

optical lenses

recirculating tube for water-bath

hinge

syringe pump

(a)

(b)

(c)

FIGURE 1 (a) A schematic of the experimental setup. (b) A section of the channel. (c) O-rings placed at the end of each channel section for the sealing [Color figure can be viewed at wileyonlinelibrary.com]

and Morris[42], Figure 6 with $\dot{\gamma}_{NL} = \epsilon^2$. In the present work, we have considered $\phi_m = 0.6$, and the regularization parameter as $\epsilon = 10^{-5}$.

We report our results in dimensionless form and adopt a Cartesian coordinate system shown in Figure 1a. The axes are scaled with the dimensions of the setup, that is, $\hat{L}, \hat{D}, \hat{H}$.

3 | METHODOLOGY

This section explains our experimental methodology. That includes the channel setup, visualization system, test fluids and particles, experimental procedure, and image analysis.

FIGURE 2 The raw images of the suspension flow at the beginning and the end of the channel setup for different bulk solid volume fractions

$\overline{\phi}_b = 0.1$

$\overline{\phi}_b = 0.2$

$\overline{\phi}_b = 0.3$

$\overline{\phi}_b = 0.4$

$\overline{\phi}_b = 0.5$

$x = 0.009$ $x = 0.971$
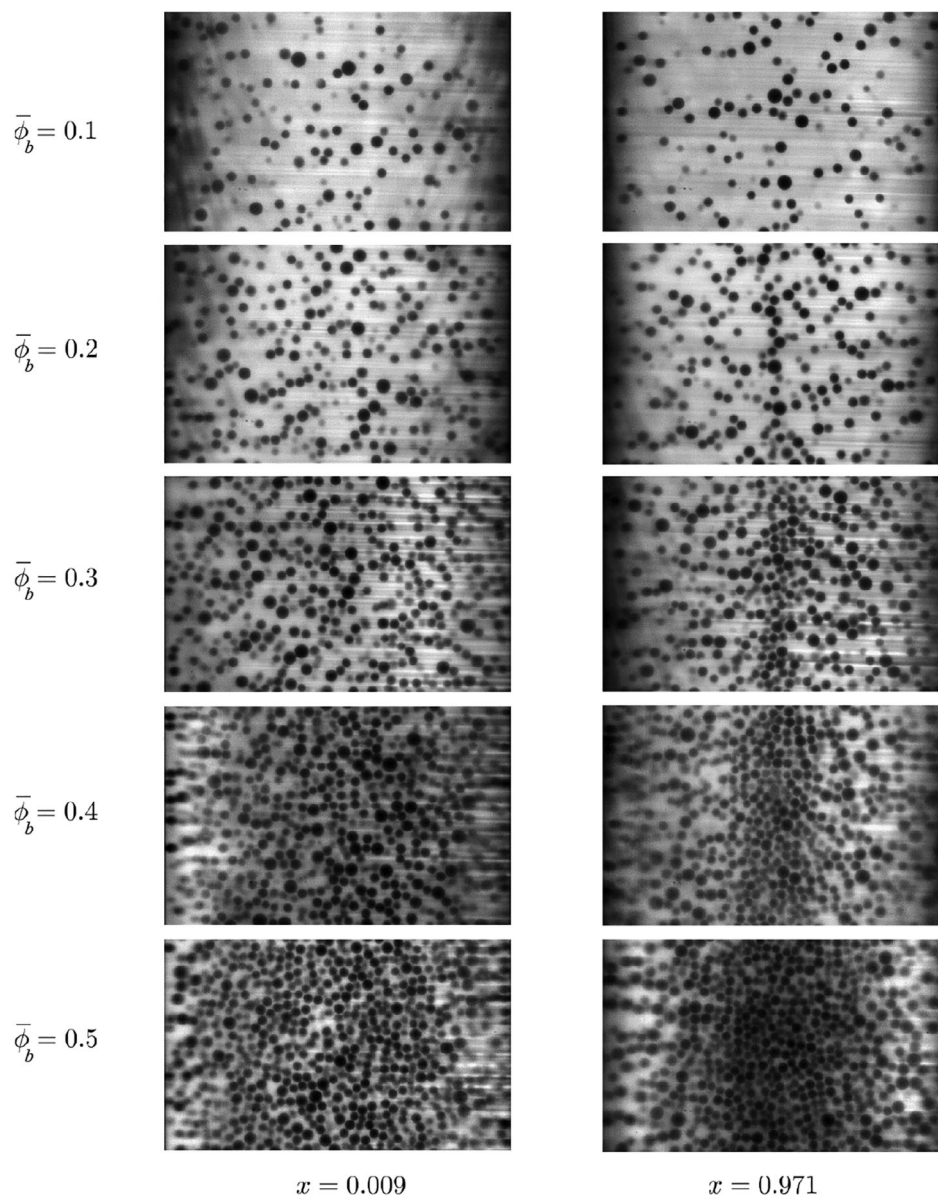
3.1 | Experimental setup

As explained in Section 2 (see also Table 1), a channel setup resembling a fracture requires a length that is three orders of magnitude larger than the width. The dimension requirements of the channel make the tolerance extremely small on all dimensions. Moreover, we want to build the channel using transparent acrylic materials to be able to visualize the flow. Maintaining the tolerances while machining the acrylic (poly methyl methacrylate [PMMA]) materials is extremely difficult. These tolerances cannot be maintained on extremely long pieces of acrylic due to the variance in the stock itself. Therefore, we constructed the channel out of 20 smaller and more accurate channel sections. The length of each section is 20 cm. Figure 1b shows one of the sections that includes three channels. A central channel (2 mm width) for the suspension to flow and two side channels (3 mm width)

to recirculate water for controlling the temperature of the suspension and consequently its RI.

The sections of channel are precisely aligned and sealed together and the O-rings between the sections prevent possible leakages (see Figure 1c). The setup, shown in Figure 1a, is then mounted on a RPR-416-12 RPR reliance optical tabletop purchased from Newport. The tabletop is 0.3048 m thick with a 1.2192 m width, a 4.8768 m length, and M6 × 1 holes on a 0.0254 m grid. The S-2000A-423.5 stabilizer set was also purchased from Newport to support the tabletop. This stabilizer set consists of four vibration dampening legs that the tabletop is connected to. This set up provides a completely flat and vibration free area for the channel to sit.

We use a precision syringe pump (two high-pressure modules purchased from neMESYS GmbH) to pump the suspension in the central channel and simultaneously we recirculate water in the side channels using a water bath.
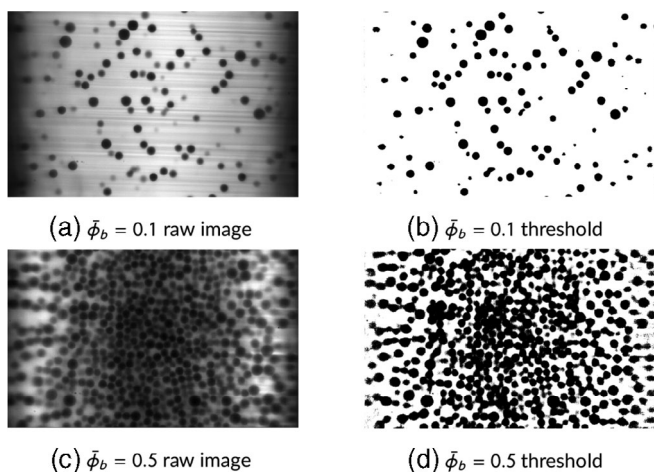
(a) $\bar{\phi}_b = 0.1$ raw image

(b) $\bar{\phi}_b = 0.1$ threshold

(c) $\bar{\phi}_b = 0.5$ raw image

(d) $\bar{\phi}_b = 0.5$ threshold

FIGURE 3 Image processing of particles suspended in the Newtonian fluid; (a) a raw image sample at $\bar{\phi}_b = 0.1$; (b) the threshold of the sample image at $\bar{\phi}_b = 0.1$; (c) the raw image sample at $\bar{\phi}_b = 0.5$; and (d) the threshold of the sample image at $\bar{\phi}_b = 0.5$
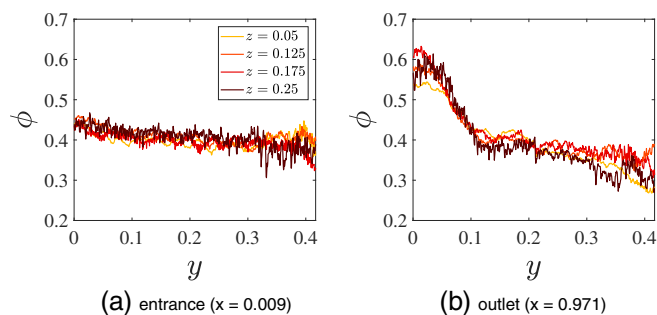

(a) entrance (x = 0.009)

(b) outlet (x = 0.971)

FIGURE 4 The particle concentration profiles at different channel's height (direction z) plotted across the gap (a) the inlet, (b) the outlet of the channel. The bulk volume fraction is $\bar{\phi}_b = 0.4$ [Color figure can be viewed at wileyonlinelibrary.com]

3.2 | Test particles and fluids

We make a transparent model suspension consisting of non-Brownian particles and Newtonian suspending fluids as follows. PMMA particles are used with the diameter in the range of 75–90 μm. The density and RI of PMMA particles are $\rho = 1.19$ g/ml and $n = 1.49$, respectively. The fluid for the Newtonian suspension is similar to what Pham used.[46] It is a combination of Triton x-100(76 wt%), zinc Chloride (14.9 wt%), water(9 wt%), and hydrochloric acid(0.1 wt%). The viscosity is 4.64 Pa.s. The weight fractions are defined in a way to match the density and RI of PMMA particles. To recognize PMMA particles from the fluid during the imaging, a fluorescent dye (rhodamine 6G) is mixed with the fluid phase with a concentration of 3 mg/L. The dye concentration is set to optimize the contrast between the solid and liquid phases. The temperature of the set-up is set to 30 ± 0.1°C in order to maximize RI matching between the solid and fluid phases (within 10^{-4}). This suspension is the same as that used by Snook et al.[20] and Sarabian et al.[10] Sarabian et al.[10] have shown that its

rheological behavior is fairly modeled by the Morris and Boulay[43] laws presented is Section 2.

For each experiment, we make 1,300 ml of the suspension and we take the following steps. First, the particles are washed using an ultrasonic water bath. Then, the particles are placed in the oven at 50°C for 48 hr to ensure that they are completely dried. The particles and the fluid are mixed for 3 hr to be completely homogenized. The prepared suspension is left in a closed and sealed container (with almost no evaporation) for 24 hr to make sure the bubbles are removed.

3.3 | Experimental procedure

We pour the suspension in a reservoir very gently to avoid trapping bubbles. We load the syringe pumps with the suspension from the reservoir. The syringe pumps operate at the flow rate of 0.01 ml/s, draw the suspension from the reservoir, and send it to the channel. We designed a plumbing system to recirculate the suspension to the reservoir. A perforated blade is machined and placed in the reservoir to homogenize the suspension gently. The plumbing system consists of tubes and ball valves made of Polyoxymethylene material purchased from Advanced Technology products.

The circulating water bath pumps the water through the side channels and maintains the temperature at 30 ± 0.1°C to maximize the RI matching between the solid and the fluid phases. Experiments are performed at five different bulk volume fractions of $\bar{\phi}_b = 0.1$, 0.2, 0.3, 0.4, and 0.5. We built an optical setup to scan the channel vertically by taking images from the top to the middle plane. The optical setup is mounted on a rail system and moved along the channel to scan the axial development of the flow. Section 3.4 explains the details of the optical system.

After finishing the experiment, we remove the pumps and the tubing, and we tilt the channel using two gas spring jacks. It takes about 2 days for the suspension to drain gradually. We collect the suspension and wash the particles with a large amount of water to remove the suspending fluid. We use an ultrasonic water bath to remove any possible residue of the suspending fluid from the particles to be able to reuse them. The channel is washed with the filtered water to remove all the residues of the suspension, and it is then air-dried for several days.

It is noteworthy to mention that the current data reported for each bulk volume fraction required about 60 days of performing an experiment, which includes preparing the materials, conducting the test, scanning the setup, draining, cleaning, and washing the setup. Scanning the setup itself included a loop of examining the quality of images, tuning the optical setup, and temperature for that specific experiment, and rescanning until achieving the best quality images. These tasks exclude the time and effort of designing and building the setup and in-house optical system.

FIGURE 5 Particle concentration profiles at the end of the channel at (a) $\bar{\phi}_b = 0.1$, (b) $\bar{\phi}_b = 0.2$, (c) $\bar{\phi}_b = 0.3$, (d) $\bar{\phi}_b = 0.4$, and (e) $\bar{\phi}_b = 0.5$. The measurements are compared with the experimental studies of Koh et al.,[21] Lyon and Leal,[22] two-dimensional suspension balance model (SBM) prediction with the rheological law of Morris and Boulay,[43] three-dimensional SBM results of Miller and Morris,[42] and simulations of Yeo and Maxey.[36] The data of Miller and Morris[42] correspond to Figure 6 of their paper with $\dot{\gamma}_{NL} = \epsilon^2$ [Color figure can be viewed at wileyonlinelibrary.com]
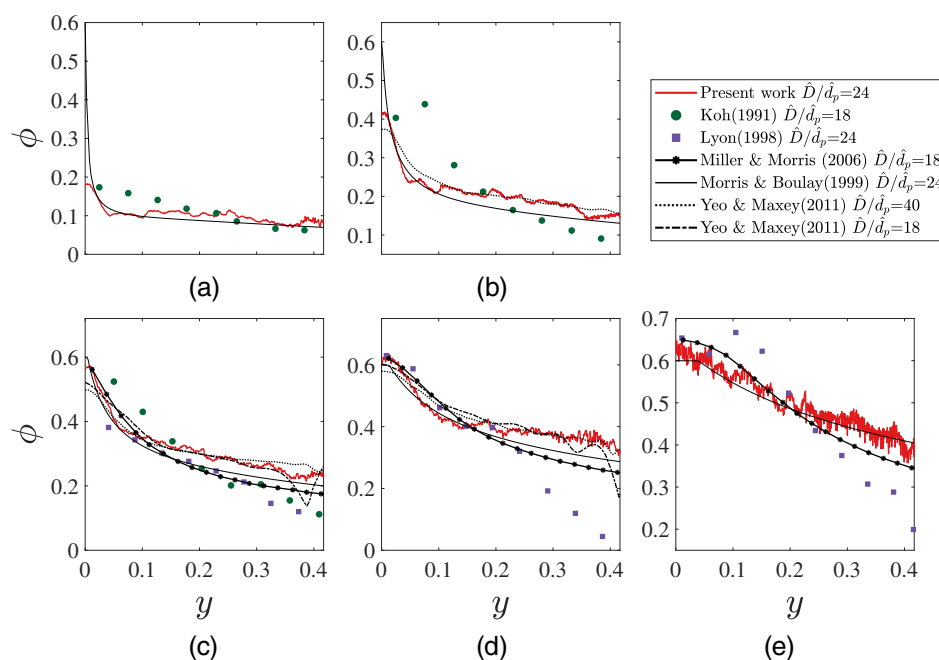
3.4 | Optical setup

We use the RI matching technique to visualize the suspension flow. The optical setup is illustrated in Figure 1a. A semiconductor green laser diode of 200 mW power and wavelength of 532 nm is used as the light source. The laser passes through a vertical plano-convex cylindrical lens with a focal length of ($f = 10$ mm) to make a horizontal laser sheet. The diverging laser sheet goes through a vertical plano-convex cylindrical lens with a focal length of ($f = 100$ mm) to collimate the laser sheet. A horizontal plano-convex cylindrical lens with a focal length of ($f = 50$ mm) is used to thin the laser sheet thickness (≈ 15 μm).[47,48]

The suspending fluid contains rhodamine 6G, which illuminates under the laser diode projection. The concentration of rhodamine is chosen to be 3 mg/L to optimize the contrast between the particles and fluid all over the gap. The fluorescent dye absorbs 524 nm (green) wavelength laser light and emits it at 566 nm. Since the suspension is transparent, the light can go through without diffraction. A 2-megapixel CCD camera (purchased from Basler) mounted on top of the channel receives the light from the suspending fluid. A macro lens (purchased from Sigma-Photos) is mounted on the CCD camera to be able to visualize small particles of the diameter of 60 μm and above. A high pass filter (550 nm filter purchased from Thorlabs) is mounted between the camera and channel to remove the noise. The particles are not covered with fluorescent dye; therefore, a contrast forms between the particle phase and the fluid phase and makes it possible to visualize the suspended particles.

This optical system allows us to take high quality images of the suspension flows. The exposure time of the camera is set to be 20 ms and 100 images are taken at each location. The laser power is set to be 80% of the capacity of a 200 mW laser generator. The laser power is tuned to have enough light in the camera sensor and also avoid bleaching the dye in the fluid. A typical example of images is shown in Figure 2. The images correspond to the plane located in the middle of the height of the channel. The distribution of particles at the inlet and outlet experimental windows is shown. For all of the solid volume fractions, the suspension is homogeneous at the entrance. However, at the outlet, the solid volume fraction is inhomogeneous due to the migration of particles from the walls to the center of the channel.

3.5 | Image analysis

The key factors in successful computation of the local solid volume fraction are first to accurately discern each particle in the image plane, and second to retain the particle shape. In particular, the latter factor is crucial to extract the particle concentration profiles and particle velocity by the means of circular Hough transform which was previously adopted by Sarabian et al.[10] and Snook et al.,[20] respectively. In this study, we compute the solid volume fractions in several steps. First, the image contrast is enhanced to distinguish particles from the background fluid by computing several histograms, each corresponding to a separate part of the image, and uses them to redistribute the intensity values of the image. Next, a threshold was calculated which implements the Li method[49] that is an iterative method based on the minimum cross-entropy thresholding using ImageJ.[50] In this method, a threshold level is computed by minimizing the spread function from the foreground and background classes. Once the optimization procedure is over and the threshold level is found from the iterative algorithm, then we filter the image by allocating pixel intensity values smaller than the threshold level as black, and the rest as white. Figure 3 depicts typical examples of an image before and after applying the threshold at two different bulk volume fractions. The resulting image out of this step is a binary image and we can easily

infer the solid volume fraction by accounting the black pixels as particles and white pixels as background fluid.

Particle image velocimetry (PIV) is performed to measure the particle velocity U_p from successive images recorded from the suspension flow at 0.1 s time intervals. The velocity field is calculated in the shear plane (*xy* plane) and then averaged in the *x* direction to compute the velocity profile. For more information on the PIV procedure, the

readers are referred to the work of Firouznia et al.[41] MatPIV[51] was employed to analyze the pairs of images. Each image is divided into subimages (interrogation windows) with overlap of 50%. The PIV algorithm uses two successive images and takes the corresponding interrogation windows in order to perform cross correlation and compute the velocity field. The PIV algorithm iterates the cross correlation twice with the window sizes of 64 × 64 and 32 × 32 pixels to improve
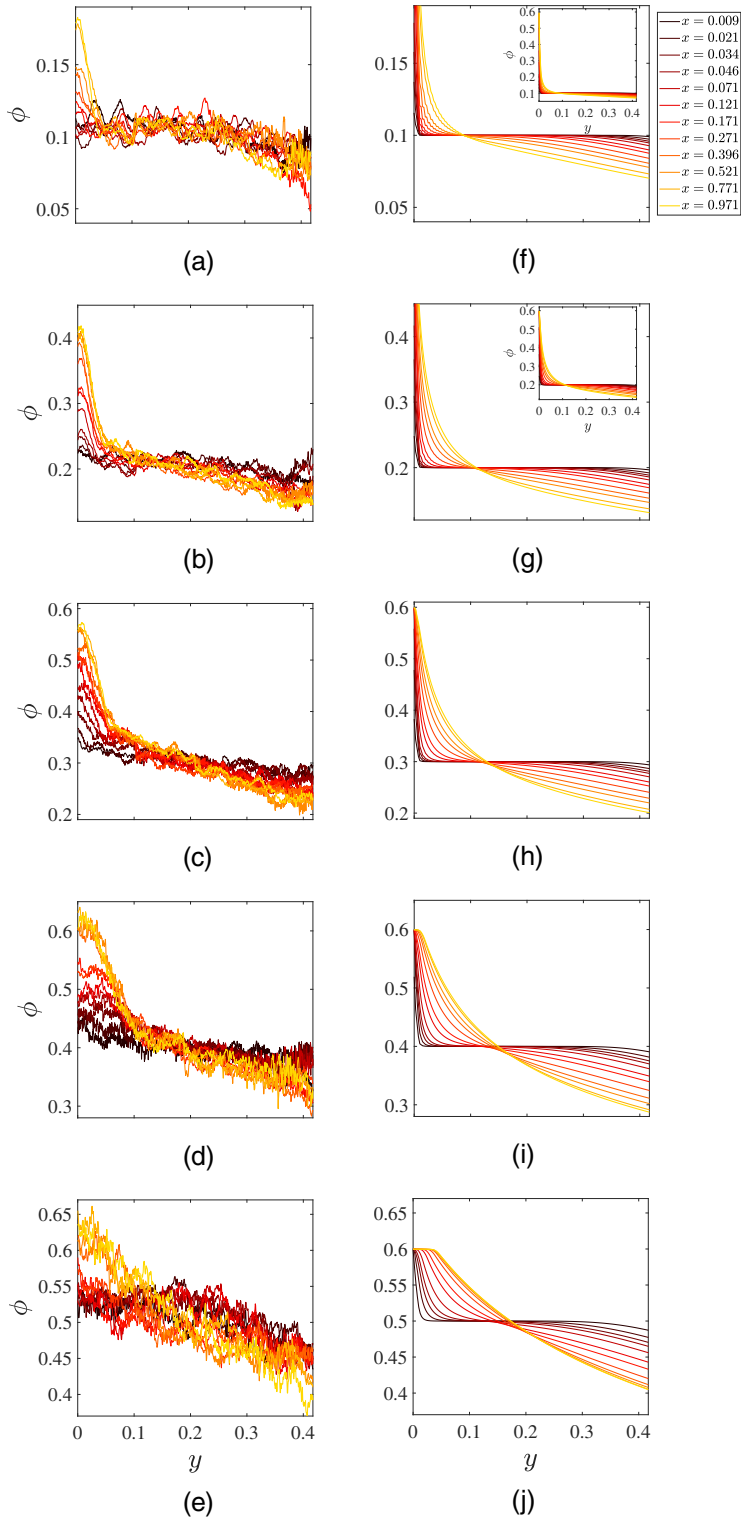

FIGURE 6 Axial evolution of the particle concentration for present work at different bulk volume fractions of (a) $\bar{\phi}_b = 0.1$, (b) $\bar{\phi}_b = 0.2$, (c) $\bar{\phi}_b = 0.3$, (d) $\bar{\phi}_b = 0.4$, and (e) $\bar{\phi}_b = 0.5$. Evolution of the particle concentration for the two-dimensional suspension balance model (SBM) prediction with the rheological laws of Morris and Boulay[43] at different bulk volume fractions of (f) $\bar{\phi}_b = 0.1$, (g) $\bar{\phi}_b = 0.2$, (h) $\bar{\phi}_b = 0.3$, (i) $\bar{\phi}_b = 0.4$, and (j) $\bar{\phi}_b = 0.5$ [Color figure can be viewed at wileyonlinelibrary.com]

the accuracy. Several filters such as signal to noise ratio (SNR) are used to identify the false vectors. The false vectors are removed and replaced by linear interpolation between the neighboring vectors.

4 | RESULTS AND DISCUSSION

In this section, we present the experimental measurements of the velocity profile of the suspension as well as the solid volume fraction at different parts along the channel. We also compare our results with the SBM and some available experimental and computational data.

As discussed in Section 2, from the small width to height ratio of our channel, the central part of the channel flow can be approximated as a 2D flow. Therefore, the boundary effects in the vertical direction (z direction) are insignificant. We examine this point by measuring the concentration profile across the width of the channel (y direction) at different locations along the z axis. Figure 4a,b illustrates the particle volume fraction close to the entrance ($x = 0.009$) and outlet ($x = 0.971$), respectively. The results correspond to the experiment with $\bar{\phi}_b = 0.4$.

Several features are evident. First, we note that the variation of ϕ along the vertical direction z is insignificant compared to the change of ϕ across the width y. Second, the concentration profile is symmetric around $y = 0$ due to the setup's geometrical symmetry. Therefore, we merely show our measurements in half of the width. The results validate our assertion in Section 2 that the flow is 2D (in the xy plane) and the vertical boundary effects are negligible on the suspension dynamics from $z \geq 0.125$. This justifies comparing our data with the solution of the 2D SBM problem.

It is noteworthy to mention that we were unable to compute the solid volume fraction in the narrow region close to the solid walls, that is, in $0.4 < y \leq 0.5$. However, the velocity profile of the particle phase can be measured in the whole gap (shown later). The slight and invisible residue of glues used for constructing the channel affects the quality of the image. Therefore, close to the walls, there exist streaks lowering the SNR. The streaks close to the walls can be seen in the raw images shown in Figure 2. Consequently, in this paper, we only report the volume fraction measurements in $0 \leq y \leq 0.4$.

Figure 5 demonstrates the particle concentration profiles at the end of the channel at different bulk volume fractions. The fully developed concentration profiles are computed near the channel outlet, at $x = 0.971$. For all the bulk volume fractions, the concentration profiles indicate the migration of particles from the walls (high-shear-rate region) toward the channel centerline (zero-shear-rate zone). Besides, we observe that maximum particle volume fraction, which occurs at the channel centerline ($y = 0$), increases with the bulk volume fraction. For those experiments with $\bar{\phi}_b \gtrsim 0.3$, the maximum value of ϕ is about 0.6 at the center of the channel. This behavior is consistent with the solution of Equation (10). At the fully developed state, the left hand side of the equation is zero implying that Σ_p is constant across the channel. A nonzero constant value of Σ_p at the center of the channel, where the shear rate is zero, is possible if the viscosity of the suspension diverges. This singular behavior occurs at the limit of jamming
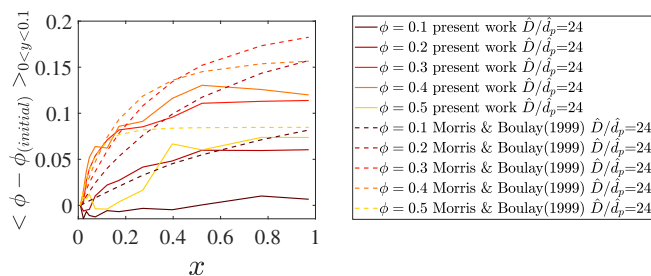

FIGURE 7 The spatially averaged $\phi - \phi_{initial}$ from $y = 0$ to $y = 0.10$ versus x [Color figure can be viewed at wileyonlinelibrary.com]
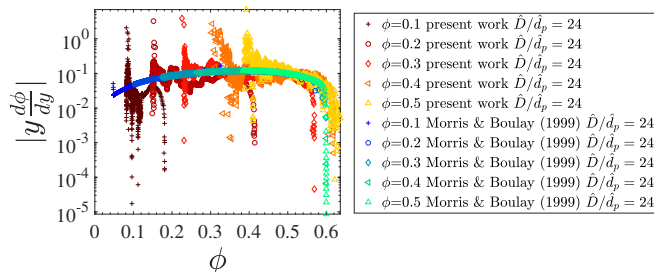

FIGURE 8 A comparison between the present work and the two-dimensional suspension balance model (SBM) prediction (rheological law of Morris and Boulay[43]) for the dimensionless concentration gradient in the channel flow [Color figure can be viewed at wileyonlinelibrary.com]

volume fraction, that is, $\phi \rightarrow \phi_m$. Therefore, the trends of solid volume fraction profiles for $\bar{\phi}_b \gtrsim 0.3$ follow the prediction of the dimensionless governing equations, which are based on the SBM. It has been shown that the value of ϕ_m is around 0.585 by several researchers (see, e.g., [35] and Guazzelli and Pouliquen[6]). Consistently, our results show that the central value of ϕ that corresponds to the maximum packing volume fraction is about 0.6.

Another important observation is that in the dilute suspension regime, that is, at $\bar{\phi} \lesssim 0.3$, the value of the particle volume fraction ϕ at the channel center is less than the maximum packing fraction ϕ_m. This observation is not consistent with the prediction of the SBM and, more specifically, the solution to Equation (11). As explained above, according to the SBM, the solid volume fraction should approach ϕ_m at the center of the channel where the shear rate is zero. This prediction is independent of the value of $\bar{\phi}_b$. It is in contrast with what we observe in our experimental measurements. Indeed, based on Figure 5a,b, ϕ does not reach to ϕ_m at $y = 0$, but to a value that is an increasing function of $\bar{\phi}_b$. Recently, several other experimental observations have been reported that do not follow the SBM's prediction, calling for the theoretical and numerical studies to improve the model framework for the non-Brownian suspensions.[10,16]

Moreover, we observe that the maximum variation of ϕ across the channel occurs for the experiments with $\bar{\phi}_b \tilde{} 0.3$. Therefore, the migration amplitude exhibits a nonmonotonic behavior with the bulk
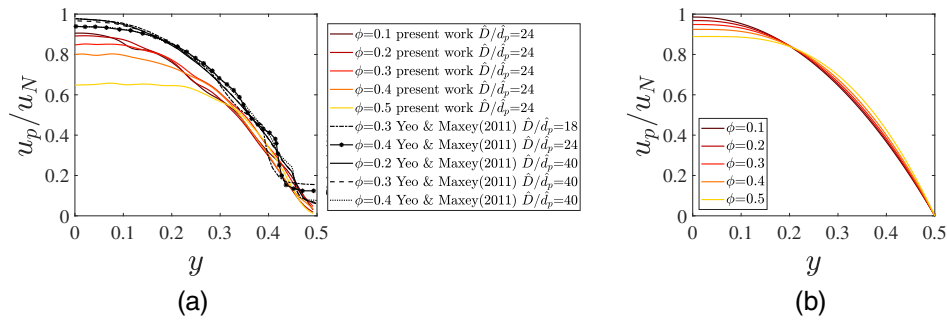
FIGURE 9 (a) The particle phase velocity at the end of the channel normalized by theoretical velocity for Newtonian fluid at the center with the same condition at different bulk volume fractions $\bar{\phi}_b$ for present work and simulations of Yeo and Maxey[36]; (b) The steady-state suspension velocity at different bulk volume fractions $\bar{\phi}_b$ for suspension balance model (SBM) prediction with rheological law of Morris and Boulay $\hat{D}/\hat{d}_p = 24$ [43] [Color figure can be viewed at wileyonlinelibrary.com]
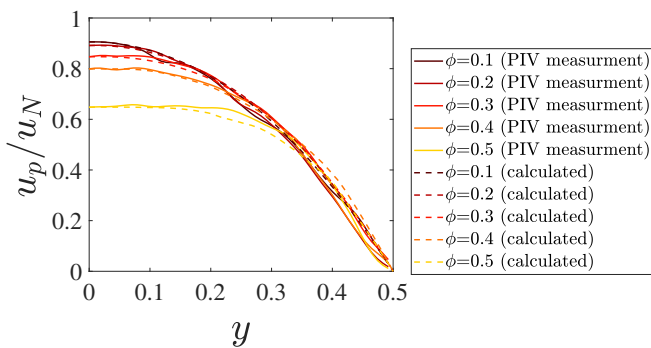

FIGURE 10 The particle phase velocity at the end of the channel normalized by theoretical velocity for Newtonian fluid at the center with the same condition at different bulk volume fractions $\bar{\phi}_b$ obtained from particle image velocimetry (PIV) measurements and the calculated velocity from the distribution of solid volume fractions [Color figure can be viewed at wileyonlinelibrary.com]

volume fraction. We have also shown the nonmonotonic trend in our recent work concerning the suspension flows in a wide-gap Taylor–Couette cell.[10]

We have compared the particle concentration profiles at the end of the channel with the available experimental and computational studies in Figure 5. According to the figure, the previous experiments of Koh et al.[21] and Lyon and Leal[22] performed in a rectangular channel are in agreement with our measurements qualitatively in the core region, that is, far from the walls and the center of the channel. However, the experiments of Lyon and Leal[22] at $\bar{\phi}_b = 0.4$ fails to correctly measure the particle concentration in the vicinity of the channel wall. The discrepancy might be due to the loss of signal near the boundaries in the LDV technique.

We find that the direct numerical simulations (DNS) of Yeo and Maxey[36] follow our experimental measurements. The shape of concentration profiles is fairly similar. Moreover, the maximum concentration at the channel center is below ϕ_m for $\phi_b = 0.2$ and 0.3, and of same order of magnitude as in our experiments. For $\phi_b = 0.4$, ϕ_m is reached at the middle in both our experiments and the simulations. It is noteworthy to mention that Yeo and Maxey[36] have studied the

flow for three different confinement ratios (ratio between the channel width to the particle diameter $\hat{D}/\hat{d}_p$). The numerical results show the particle layering close to the walls for $\hat{D}/\hat{d}_p = 18$ and $\hat{D}/\hat{d}_p = 24$. We have recently addressed the layering effect and explained it is associated with the discrete effect and crystallization of the particles close to the boundaries. We have shown that the particle layering does not affect the fully developed concentration profiles averaged over a broader neighborhood.[10]

Our experimental observations are not entirely consistent with the SBM framework, particularly as we approach the channel's center for $\bar{\phi}_b \lesssim 0.3$. The model results in cusps forming in the central regions where the solid volume fraction approaches ϕ_m. Nott and Brady[30] proposed a resolution for resolving the cusp via including the nonlocal effects. They suggested adding an equation for the granular temperature to the system of the equations. The diffusion of the granular temperature results in a blunter solid volume fraction profile and removal of the cusp. Nonetheless, the discrepancy between the prediction of SBM and our experimental data for $\bar{\phi}_b \lesssim 0.3$ in the central region is more than the value of nonlocal's resolution given in Reference 30.

The novelty of our setup enables us to measure the axial development of the solid volume fraction experimentally for the first time. We report the particle concentration profiles at different locations as we march along with the flow, x direction. Figure 6a–e shows the results of our experimental observations for different values of $\bar{\phi}_b$.

The particle migration can be clearly observed by the increase in particle volume fraction ϕ at the center of the channel ($y = 0$) and its decrease near the edges ($y = 0.4$). Furthermore, we observe that the migration occurs faster at larger bulk volume fraction $\bar{\phi}_b$, that is, the particle concentration reaches its fully developed state at a smaller length along the flow direction x. The reduction of steady-state length scale by bulk volume fraction enhancement is in agreement with the SBM framework[30] and can be explained via Equation (11). Indeed, a balance of the right-hand side and left-hand side of this equation implies that the fully developed length, x, scales inversely with ($f(\phi)/\phi)) \times \Sigma_p(\phi)$. The latter is an increasing function of $\bar{\phi}_b$ resulting in a shorter fully developed length as $\bar{\phi}_b$ increases.

The predictions of the nearly one-dimensional Equation (11) with the Morris and Boulay[43] laws are presented in Figure 6f–j for the

same x and $\bar{\phi}_b$ values as for the experimental data of Figure 6a–e. The shape of the curve and their evolution with x are in fair agreement with the data. We note that the central region's size where most of the particles accumulate is of the same order of magnitude in both the experiments and the model. This region grows with $\bar{\phi}_b$. As noted above, the main discrepancy is that the volume fraction always reaches ϕ_m at the center in the model, which is not the case at low $\bar{\phi}_b$ in experiments.

To better characterize the axial development of the volume fraction profiles, we compute the average of $\phi - \phi_{\text{initial}}$ over the central region (from $y = 0$ to $y = 0.10$). Figure 7 shows the experimental data and solution of Equation (11) follow the same shape. However, the migration is slower in the experiments for $\phi_b = 0.5$. This plot allows us to provide a crude estimate of the order of magnitude of x for the fully developed state which is found to be of order 0.8 for $\bar{\phi}_b = 0.1$, of order 0.5 for $\bar{\phi}_b = 0.2$, $\bar{\phi}_b = 0.3$, and $\bar{\phi}_b = 0.4$, and of order 0.4 for $\bar{\phi}_b = 0.5$. It is impossible to report more accurate values as it would require scanning the whole channel and an extremely long time to run the experiment.

The steady-state data can be presented differently for the purpose of the comparison with constitutive equations. As pointed out by Ramachandran and Leighton,[52] the dimensionless gradient $y(d\phi/dy)$ in the fully developed state should be a function only of the concentration. Figure 8 shows the comparison between the present work and the SBM prediction (rheological law of Morris and Boulay[43]) of the dimensionless concentration gradient in the channel flow. The results show that the dimensionless gradient is only a function of concentration. All data fall on a master curve, except for those at the center of the channel. In this region, the data show an abrupt jump to zero. Such a trend points to the breakdown of the continuum modeling in the central region. This plot also confirms the fair agreement with the Morris and Boulay model.

Finally, we discuss the velocity profiles. Figure 9 presents the measurements of the particle phase velocity close to the outlet for different bulk volume fractions. We normalize the velocity profiles with the value of the velocity at the center for a Newtonian fluid. u_p is the particle phase velocity that is measured from the experiment, and u_N is the theoretical velocity for Newtonian fluid at the center of the channel with the same condition. The results show that the velocity evolves toward a blunt profile as we increase the bulk volume fractions $\bar{\phi}_b$. This trend is similar to the prediction of the SBM for the suspension velocity profile (see Figure 9b). As far as the particle phase velocity is concerned, we have compare our results with that of Yeo and Maxey.[36] Figure 9a shows that the experimental velocity profiles have smaller magnitudes compare to those computed from the Numerical simulations.

Here, we show the consistency between the steady-state volume fraction profiles, the steady-state velocity profiles, and the continuum modeling. To this end, we have computed the velocity profiles from the measurements of $\phi(y)$ using $\eta(\phi)$ from the rheological law of Morris and Boulay.[43] In the central plane of the channel, suspension shear stress at steady state is $\tau \propto y$. Therefore, we can compute the shear rate as $\dot{\gamma}(y) = \tau(y)/\eta(\phi(y)) \propto y/\eta(\phi(y))$. Then, the velocity profile can

be computed by integrating the shear rate. In the absence of a pressure drop measurement, the velocity can then be known only up to a constant. We match the computed velocity at the center with our PIV measurements. Figure 10 shows a good agreement between these two velocity profiles. This agreement implies the viscosity function $\eta(\phi)$ chosen to compute the velocity profile from ϕ measurements accounts correctly for the material behavior.

5 | SUMMARY

A high precision rectangular channel is designed to experimentally study the evolution of the solid volume fraction in fracturing flows. We conducted experiments to study the shear-induced migration of rigid spheres in a Newtonian fluid, in the Stokesian regime. We adopted a highly resolved index-matching technique and PIV to calculate the solid volume fraction profiles and the particle phase velocity, respectively. Well-controlled experiments were performed for a wide range of bulk volume fractions ranging from 0.1 to 0.5 to cover the whole range of dilute to dense suspension flows. Fully developed concentration profiles, along with the axial developments and migration dynamics were analyzed and compared with the existing experimental and computational studies.

We find that the maximum particle volume fraction, which occurs at the channel centerline, increases with the bulk volume fraction and eventually gets saturated to a value of 0.6 for $\bar{\phi}_b \gtrsim 0.3$. Overall, the SBM with the Morris and Boulay law provides a fair description of the migration profiles and of their axial development. However, there exist discrepancies between our experimental data and the prediction of the SBM framework. One difference is that the SBM predicts that the local particle concentration reaches the maximum packing fraction ϕ_m at the channel centerline regardless of the value of the bulk volume fraction.

Besides, we compared some of our experimental data with the available experimental and computational results. We showed that the concentration profiles shapes resulted from fully three-dimensional numerical simulations performed in a channel flow by Yeo and Maxey[36] are fairly similar to our results, and the maximum concentration at the channel center is of same order. In these well-resolved simulations, the authors considered the discrete effect resulting from the confinement and finite-size of the particles, which is more pronounced at the larger bulk volume fraction. Here, we tried to minimize these effects by performing our experiments for the largest possible confinement ratio, $\hat{D}/\hat{d}_p = 24$. Although there exist particle layering close to the boundaries, we could not measure it in this work due to the low SNR.

Furthermore, we find that our measurements are in qualitative agreement with the previous experimental study of Koh et al.[21] and Lyon and Leal[22] in the core region (far from the center and solid walls). Nonetheless, their fully developed particle volume fraction measurements deviate from ours in the vicinity of walls and near the channel centerline. It might be due to the signal loss in the LDV technique close to the channel walls as the solid volume fraction decreases. In

Koh's experiments,[21] the particle size and channel length were kept fixed and the confinement ratio ($\hat{D}/\hat{d}_p$) was varied by changing the channel width.

The unique feature of our setup in resembling a long and thin fracture allows us to provide data on the axial development of the solid volume fraction for both dilute and dense flow of suspensions. We showed the evolution of ϕ along the flow direction x, that is, from the inlet to the outlet of the channel.

Finally, we have performed a PIV analysis to measure the particle phase velocity. We observed that the particle phase velocity profiles evolve from a parabolic shape to a plug shape by increasing the bulk volume fraction $\bar{\phi}_b$. It is expected as the solution to the velocity profile is coupled to the solid volume fraction exhibiting a blunter profile, in the core region of the channel flow, for larger values of $\bar{\phi}_b$. Also, we observed a good agreement between the measured velocity profiles from PIV with the velocity profiles calculated from the measured concentration profiles.

The highly resolved experimental data presented in this study provides an insight into understanding the dispersion of solids in fracturing flows of petroleum industries. In the near future, we will provide more experimental data on the effect of boundaries, crystallization, dynamics, solid inhomogeneities, and non-Newtonian interstitial fluid. Our experimental effort along with the recent work of other researchers in the field, for example, [10,16,19,20,31] may provide a basis for improving the continuum model frameworks explaining the flows of non-Brownian suspensions.

AUTHOR CONTRIBUTIONS

Ahmadreza Rashedi: Writing-original draft. **Mohammad Sarabian:** Writing-original draft. **Mohammadhossein Firouznia:** Writing-original draft. **Dallas Roberts:** Writing-original draft. **Guillaume Ovarlez:** Writing-original draft. **Sarah Hormozi:** Writing-original draft.

ORCID

Guillaume Ovarlez [ID] https://orcid.org/0000-0003-1554-1080
Sarah Hormozi [ID] https://orcid.org/0000-0001-5712-1178

REFERENCES

1. EIA U. Hydraulic fracturing accounts for about half of current US crude oil production; 2016.

2. EIA U. Hydraulically fractured wells provide two-thirds of US natural gas production; 2016.

3. Gillard MR, Medvedev OO, Hosein PR, Medvedev A, Peñacorada F, d'Huteau E, et al. A new approach to generating fracture conductivity. In: SPE Annual Technical Conference and Exhibition Society of Petroleum Engineers; 2010. .

4. Huang B, Liu C, Fu J, Guan H. Hydraulic fracturing after water pressure control blasting for increased fracturing. *Int J Rock Mech Mining Sci.* 2011;48(6):976-983.

5. Hormozi S, Frigaard I. Dispersion of solids in fracturing flows of yield stress fluids. *J Fluid Mech.* 2017;830:93-137.

6. Guazzelli E, Pouliquen O. Rheology of dense granular suspensions. *J Fluid Mech.* 2018;852.

7. Guazzelli E, Morris JF. *A physical introduction to suspension dynamics.* Vol 45. UK: Cambridge University Press; 2011.

8. Leighton D, Acrivos A. The shear-induced migration of particles in concentrated suspensions. *J Fluid Mech.* 1987;181:415-439.

9. Phillips RJ, Armstrong RC, Brown RA, Graham AL, Abbott JR. A constitutive equation for concentrated suspensions that accounts for shear-induced particle migration. *Phys Fluids A: Fluid Dyn.* 1992;4(1):30-40.

10. Sarabian M, Firouznia M, Metzger B, Hormozi S. Fully developed and transient concentration profiles of particulate suspensions sheared in a cylindrical Couette cell. *J Fluid Mech.* 2019;862:659-671.

11. Gadala-Maria F, Acrivos A. Shear-induced structure in a concentrated suspension of solid spheres. *J Rheol.* 1980;24(6):799-814.

12. Abbott J, Tetlow N, Graham A, et al. Experimental observations of particle migration in concentrated suspensions: Couette flow. *J Rheol.* 1991;35(5):773-795.

13. Chow AW, Sinton SW, Iwamiya JH, Stephens TS. Shear-induced particle migration in Couette and parallel-plate viscometers: NMR imaging and stress measurements. *Phys Fluids.* 1994;6(8):2561-2576.

14. Ovarlez G, Bertrand F, Rodts S. Local determination of the constitutive law of a dense suspension of noncolloidal particles through magnetic resonance imaging. *J Rheol.* 2006;50(3):259-292.

15. Bricker JM, Butler JE. Oscillatory shear of suspensions of noncolloidal particles. *J Rheol.* 2006;50(5):711-728.

16. Saint-Michel B, Manneville S, Meeker S, Ovarlez G, Bodiguel H. X-ray radiography of viscous resuspension. *Phys Fluids.* 2019;31(10):103301.

17. Karnis A, Goldsmith H, Mason S. The kinetics of flowing dispersions: I. concentrated suspensions of rigid particles. *J Colloid Interface Sci.* 1966;22(6):531-553.

18. Hampton R, Mammoli A, Graham A, Tetlow N, Altobelli S. Migration of particles undergoing pressure-driven flow in a circular conduit. *J Rheol.* 1997;41(3):621-640.

19. Oh S, Yq S, Garagash DI, Lecampion B, Desroches J. Pressure-driven suspension flow near jamming. *Phys Rev Lett.* 2015;114(8):088301.

20. Snook B, Butler JE, Guazzelli É. Dynamics of shear-induced migration of spherical particles in oscillatory pipe flow. *J Fluid Mech.* 2016;786:128-153.

21. Koh CJ, Hookham P, Leal LG. An experimental investigation of concentrated suspension flows in a rectangular channel. *J Fluid Mech.* 1994;266:1-32.

22. Lyon M, Leal L. An experimental study of the motion of concentrated suspensions in two-dimensional channel flow. Part 1. Monodisperse systems. *J Fluid Mech.* 1998;363:25-56.

23. Deshpande KV, Shapley NC. Particle migration in oscillatory torsional flows of concentrated suspensions. *J Rheol.* 2010;54(3):663-686.

24. Sarabian M, Rosti ME, Brandt L, Hormozi S. Numerical simulations of a sphere settling in simple shear flows of yield stress fluids. *J Fluid Mech.* 2020;896:A17-1-A17-42.

25. Izbassarov D, Rosti ME, Ardekani MN, et al. Computational modeling of multiphase elastoviscoplastic flows. arXiv preprint arXiv: 180309563 2018.

26. Alghalibi D, Lashgari I, Brandt L, Hormozi S. Interface-resolved simulations of particle suspensions in Newtonian, shear thinning and shear thickening carrier fluids. *J Fluid Mech*. 2018;852:329-357.

27. Izbassarov D, Rosti ME, Ardekani MN, et al. Computational modeling of multiphase viscoelastic and elastoviscoplastic flows. *Int J Numer Methods Fluids*. 2018;88(12):521-543.

28. Brady JF, Morris JF. Microstructure of strongly sheared suspensions and its impact on rheology and diffusion. *J Fluid Mech*. 1997;348:103-139.

29. Morris J, Brady J. Pressure-driven flow of a suspension: buoyancy effects. *Int J Multiph Flow*. 1998;24(1):105-130.

30. Nott PR, Brady JF. Pressure-driven flow of suspensions: simulation and theory. *J Fluid Mech*. 1994;275:157-199.

31. d'Ambrosio E, Blanc F, Lemaire E. Viscous resuspension of non-Brownian particles: determination of the concentration profiles and particle normal stresses. arXiv preprint arXiv:190701793; 2019.

32. Deboeuf A, Gauthier G, Martin J, Yurkovetsky Y, Morris JF. Particle pressure in a sheared suspension: a bridge from osmosis to granular dilatancy. *Phys Rev Lett*. 2009;102(10):108301.

33. Dbouk T, Lobry L, Lemaire E. Normal stresses in concentrated non-Brownian suspensions. *J Fluid Mech*. 2013;715:239-272.

34. Boyer F, Pouliquen O, Guazzelli É. Dense suspensions in rotating-rod flows: normal stresses and particle migration. *J Fluid Mech*. 2011;686:5-25.

35. Boyer F, Guazzelli É, Pouliquen O. Unifying suspension and granular rheology. *Phys Rev Lett*. 2011;107(18):188301.

36. Yeo K, Maxey MR. Numerical simulations of concentrated suspensions of monodisperse particles in a Poiseuille flow. *J Fluid Mech*. 2011;682:491-518.

37. Gholami M, Rashedi A, Lenoir N, Hautemayou D, Ovarlez G, Hormozi S. Time-resolved 2D concentration maps in flowing suspensions using X-ray. *J Rheol*. 2018;62(4):955-974.

38. Rashedi A, Ovarlez G, Hormozi S. Engineered transparent emulsion to optically study particulate flows in yield stress fluids. *Exp Fluids*. 2020;61(2):1-13.

39. Ovarlez G, Mahaut F, Deboeuf S, Lenoir N, Hormozi S, Chateau X. Flows of suspensions of particles in yield stress fluids. *J Rheol*. 2015;59(6):1449-1486.

40. Dagois-Bohy S, Hormozi S, Guazzelli É, Pouliquen O. Rheology of dense suspensions of non-colloidal spheres in yield-stress fluids. *J Fluid Mech*. 2015;776:R2-1-R2-10.

41. Firouznia M, Metzger B, Ovarlez G, Hormozi S. The interaction of two spherical particles in simple-shear flows of yield stress fluids. *J Non-Newton Fluid Mech*. 2018;255:19-38.

42. Miller RM, Morris JF. Normal stress-driven migration and axial development in pressure-driven flow of concentrated suspensions. *J Non-Newton Fluid Mech*. 2006;135(2–3):149-165.

43. Morris JF, Boulay F. Curvilinear flows of noncolloidal suspensions: the role of normal stresses. *J Rheol*. 1999;43(5):1213-1237.

44. Lhuillier D. Migration of rigid particles in non-Brownian viscous suspensions. *Phys Fluids*. 2009;21(2):023302.

45. Nott PR, Guazzelli E, Pouliquen O. The suspension balance model revisited. *Phys Fluids*. 2011;23(4):043304.

46. Pham PN Origin of shear-induced diffusion in particulate suspensions: crucial role of solid contacts between particles. PhD thesis, Aix-Marseille; 2016.

47. Diemunsch G, Prenel J. A compact light sheet generator for flow visualizations. *Opt Laser Technol*. 1987;19(3):141-144.

48. Prenel J, Jeudy M. A new versatile laser sheet generator for flow visualization. *Opt Laser Technol*. 1998;30(8):533-538.

49. Li CH, Lee C. Minimum cross entropy thresholding. *Pattern Recognit*. 1993;26(4):617-625.

50. Schneider CA, Rasband WS, Eliceiri KW. NIH image to ImageJ: 25 years of image analysis. *Nat Methods*. 2012;9(7):671-675.

51. Sveen JK. An introduction to MatPIV v. 1.6. 1. Preprint series Mechanics and Applied Mathematics. http://urn.nb.no/URN:NBN:no-234182004.

52. Ramachandran A, Leighton DT. The influence of secondary flows induced by normal stress differences on the shear-induced migration of particles in concentrated suspensions. *J Fluid Mech*. 2008;603:207.